JVST A
Journal of Vacuum Science & Technology A

Role of nanoscale surface defects on Sn adsorption and diffusion behavior on oxidized Nb(100)

Cite as: J. Vac. Sci. Technol. A **39**, 063212 (2021); https://doi.org/10.1116/6.0001374
Submitted: 19 August 2021 • Accepted: 27 September 2021 • Published Online: 14 October 2021

Rachael G. Farber, Sarah A. Willson and S. J. Sibener

JVST A
Journal of Vacuum Science & Technology A

ARTICLE

avs.scitation.org/journal/jva

Role of nanoscale surface defects on Sn adsorption and diffusion behavior on oxidized Nb(100)

Cite as: J. Vac. Sci. Technol. A 39, 063212 (2021); doi: 10.1116/6.0001374
Submitted: 19 August 2021 · Accepted: 27 September 2021 ·
Published Online: 14 October 2021

Rachael G. Farber, Sarah A. Willson, and S. J. Sibener[a)]

AFFILIATIONS

The James Franck Institute and Department of Chemistry, The University of Chicago, 929 E. 57th Street, Chicago, Illinois 60637

Note: This paper is a part of the Special Collection Commemorating the Career of Pat Thiel.
[a)]**Electronic mail:** s-sibener@uchicago.edu

ABSTRACT

Nanoscale structural defects such as grain boundaries, atomic dislocations, and surface roughness inhibit the stoichiometrically homogeneous growth of Nb_3Sn on Nb. This is a critical technological bottleneck for the implementation of next-generation Nb_3Sn superconducting radio frequency cavities, as thin film inhomogeneities are known to degrade superconducting properties that are essential for reaching optimal cavity performance. To determine the influence of structural defects on Nb_3Sn film growth, low and moderate surface defect densities were intentionally induced onto a (3×1)-O Nb(100) substrate, which serves as a model system to study atomic-scale Sn adsorption and diffusion. Scanning tunneling microscopy shows that, while initial Sn adsorption behavior at room temperature differs between the low and moderate defect density Nb(100) surfaces, the overall diffusion pathways at elevated temperatures are guided by the underlying oxide structure with variations resulting from increased nanoscale surface defects. The (3×1)-O Nb(100) surface with a moderate defect density also demonstrates enhanced Sn thermal stability, with the Sn desorption threshold occurring between 850 and 900 °C, approximately 50 °C higher than desorption from both the low defect density and pristine thin oxide surfaces. This suggests that structural surface defects may stabilize adsorbed Sn species on oxidized Nb at the elevated temperatures utilized in Nb_3Sn alloy growth procedures. Auger electron spectroscopy shows no significant difference in surface composition following Sn deposition at varying coverages on the pristine and defect-induced (3×1)-O Nb(100) surfaces. This indicates that the surface and near-surface composition are not influenced by the presence of nanoscale surface defects despite slight attenuations in Sn diffusion pathways on defected substrates. These results provide the first *in situ* visualization of Sn adsorption and diffusion behavior on oxidized Nb at the nanoscale, revealing the significance of the underlying Nb oxide surface structure and defect density on Nb_3Sn film growth and, ultimately, cavity performance.

I. INTRODUCTION

Nb is the current standard material for superconducting radio frequency (SRF) cavities as it has the lowest critical temperature (T_C) of all elemental superconductors ($T_C = 9.8$ K), allowing for operating temperatures of ~ 2 K.[1–3] Nb_3Sn ($T_C = 18.3$ K) has been identified as one promising SRF material, with recent efforts demonstrating Nb_3Sn SRF cavity operation at ~ 4.2 K.[4–6] This change in the operating temperature will prove crucial to the implementation of next-generation accelerators and free electron light sources due to substantially reduced costs in cryo-infrastructure.

Unlike Nb, which is malleable and can be manually formed into the desired high-, medium-, or low-velocity cavity geometry,[1,2] the brittle nature of Nb_3Sn prevents the manual formation of Nb_3Sn sheets into SRF cavities. Nb_3Sn SRF cavities must, therefore, be grown on preexisting Nb cavities, commonly *via* a Sn vapor deposition procedure.[7–9] There is a strong correlation between cavity performance and Nb_3Sn film quality. The SRF performance of Nb_3Sn thin films grown *via* vapor deposition is limited by microstructural surface inhomogeneities such as the persistence of patchy Sn-deficient regions, grain boundaries, surface roughness, and thin film areas on Nb_3Sn coated cavity coupons.[10–12] Simulations of substitutional defects such as Sn solute segregation at grain boundaries have been shown to induce flux pinning, appreciably diminishing T_C surrounding deleterious surface features on Nb_3Sn films.[4,11]

Despite attempts to advance preexisting Nb_3Sn growth procedures, fabrication of optimally performing, atomically smooth, and homogeneous Nb_3Sn films has been difficult to achieve. This has proven to be a significant barrier in implementing Nb_3Sn coated SRF cavities in superconducting particle accelerator facilities. Recent work by Posen *et al.*[13] has shown that there is a significant difference in performance between Nb_3Sn SRF cavities that are visually shiny and comprised of smaller, smoother grains compared to visually matted Nb_3Sn with larger, rougher grains. The observed results may be due to increased Sn flux during the nucleation step at 500 °C, increased Sn overpressure during cavity coating, the addition of a postfabrication nitrogen infusion step, or that the surface is comprised of thinner, smoother, smaller grains. Unfortunately, it is difficult to deconvolute the various interdependent growth parameters leading to the observed improved cavity performance.

While there have been studies investigating the relationship between Nb_3Sn film morphology and accelerating performance,[4,6,14,15] there is not a comprehensive understanding of the intermolecular interactions guiding optimally performing Nb_3Sn alloy growth. The interactions between the Nb substrate and impinging Sn atoms during Nb_3Sn growth procedures significantly influence the surface-mediated alloy growth process. Sn deposition on highly oxidized Nb terminated in the persistent bulk pentoxide (Nb_2O_5) results in distinct Sn diffusion pathways and Nb_3Sn film quality compared to Sn deposited on Nb surfaces terminated in thinner oxides or elemental Nb.[15] Specifically, it has been demonstrated that deposition on thicker Nb_2O_5 surfaces may result in enhanced Sn wetting and modify incorporation mechanisms promoting homogeneous alloy film growth with a persistent near-surface oxygen contribution.[16] Additionally, any suppression of Sn lateral diffusion required to uniformly wet the Nb surface during the initial coating steps may influence Sn diffusion into the Nb bulk during alloy formation, likely resulting in inhomogeneous Nb_3Sn grains.[15,17] Preventing the growth of inhomogeneous Nb_3Sn grains is a point of significant interest when developing modified Nb_3Sn growth procedures.[4,13,18,19] However, there is not currently a predictive Nb_3Sn growth model on oxidized Nb surfaces that details how specific morphological factors such as the Nb oxide composition, thickness, crystalline structure, and defect density influence Sn adsorption, lateral diffusion, and incorporation behavior during alloy growth.

The work presented herein investigates the structural and chemical consequences of nanoscale defects on Sn adsorption and diffusion pathways. By depositing sub-monolayer (ML) quantities of Sn onto a well characterized single crystal Nb(100) oxide reconstruction, we utilize *in situ* preparation and analysis techniques to determine the effects of defect density on Sn adsorption and diffusion pathways. The (3×1)-O/Nb(100) reconstruction is comprised of highly ordered "ladder" structures whose pristine (ρ_P) structure is modified to produce both low (ρ_L) and moderate (ρ_M) surface defect densities.[20,21] Room temperature scanning tunneling microscopy (STM) analysis of the Sn/(3×1)-O/Nb(100) samples reveals the effect of surface roughness and defect density on initial Sn adsorption and aggregation behavior. Subsequent annealing at sample temperature (T_S) equal to 500, 700, and 850 °C induces Sn diffusion on the ρ_L and ρ_M surfaces. Atomically resolved STM analysis of annealed ρ_L and ρ_M samples reveals the interplay between surface defect density and the underlying oxide structure and composition on Sn diffusion pathways. Complementary Auger electron spectroscopy (AES) analysis of ρ_P, ρ_L, and ρ_M substrates following sub-ML and multilayer Sn deposition reveals that, while the exact adsorption and diffusion pathways vary as a function of surface defect density, the surface elemental composition following Sn deposition on (3×1)-O/Nb(100) at $T_S = 24$ °C does not vary with surface defect density. This highlights the significance of controlling the underlying oxidized Nb SRF cavity surface morphology prior to the initiation of Nb_3Sn growth procedures to ensure uniform Sn adsorption and diffusion, resulting in optimally performing Nb_3Sn films.

II. EXPERIMENT

All experiments were conducted on a Nb(100) single crystal (1 cm diameter, Surface Preparation Laboratory) in an ultrahigh vacuum (UHV) system equipped with an STM chamber (UHV VT-STM, RHK Technology) and preparation chamber containing an AES analyzer, described in Veit *et al.*[20,22] A newly constructed custom deposition chamber was attached to the preexisting UHV apparatus, allowing for *in situ* Sn deposition, sample preparation, and analysis. The Sn deposition chamber, which has a base pressure of $\leq 1.0 \times 10^{-9}$ Torr, is equipped with an electron beam evaporator (EFM 3, Focus GmbH) for sub-ML precision Sn exposure, a quartz crystal microbalance (QCM, UHV Bakeable Sensor, Inficon) to calibrate Sn deposition rates, and a custom sample stage allowing for reproducible sample positioning and heating during Sn exposure.

The (3×1)-O/Nb(100) reconstruction was formed *via* repeated cycles of Ar^+ ion sputtering (1.5 keV) and annealing at a $T_S \approx 1630$ °C as measured using an infrared pyrometer (Mikron Infrared, MG-140).[12] Initial surface cleanliness was confirmed using AES, x-ray photoelectron spectroscopy, and STM analysis to confirm the presence of a pristine (3×1)-O (ρ_P) surface. Surface compositions (at. %) were obtained using the corrected AES peak-peak ratios of the differentiated spectra. STM image processing was completed using GWYDDION, an open-source scanning probe microscopy analysis software. Edge site surface area calculations and QCM Sn coverage calibrations were obtained using mask operations in GWYDDION to distinguish image pixels corresponding to specific surface features.

AES analysis of the ρ_P surface reproducibly measures 11.2 ± 1.3 at. % O and STM analysis demonstrate that 4.6 ± 1.9% of the ρ_P surface area is comprised of edge sites associated with step edges, dislocations, and adatoms. The sample was prepared as either a low defect density (ρ_L) sample, with surface defect density = 17.8 ± 1.2%, or moderate defect density (ρ_M) sample, with surface defect density = 31.3 ± 2.1%, as follows:

ρ_L sample: The ρ_P (3×1)-O surface was sputtered with Ar^+ for 15 min at 1 keV and then annealed at $T_S = 900$ °C for 15 min.

ρ_M sample: Beginning with the pristine (3×1)-O surface, the sample was sputtered with Ar^+ for 15 min at 1 keV and flashed to $T_S = 900$ °C.

Following either the ρ_L or ρ_M sample preparation, the Nb(100) sample was transferred to the deposition chamber for *in situ* Sn exposure. The EFM 3 filament conditions were monitored by the EFM 3 control box, to ensure complete melting of the 99.998–99.999% purity Sn pellets (Kurt J. Lesker) contained in the

EFM crucible. The QCM crystal and sample were positioned at the same working distance and angle with respect to the EFM crucible to ensure that a 1 cm diameter Sn vapor beam was uniformly impinged on both the sample and QCM crystal; covering the entirety of both surfaces ensured an accurate flux calibration. This allowed for the deposition rate in ng min^{-1} for specific Sn exposure fluxes to be quantified. Complementary STM data confirmed the Sn packing density on the pristine (3 × 1)-O Nb(100) surface, providing a direct conversion between deposition rate in ng min^{-1} to ML min^{-1}.

For sub-ML Sn deposition, exposure conditions were set to achieve a flux of 0.47–0.56 ML min^{-1} calibrated using QCM and STM data. The ρ_P, ρ_L, and ρ_M samples were exposed to the Sn beam for 30 s at $T_S = 24$ °C, resulting in 0.28 and 0.24 ML equivalence Sn coverage for ρ_L and ρ_M, respectively. For multilayer Sn deposition, exposure conditions were set to achieve 0.80–0.84 ML min^{-1}. The ρ_P, ρ_L, and ρ_M samples were exposed to the Sn beam for 20 min at $T_S = 24$ °C, resulting in 16.22 and 16.77 ML equivalences Sn coverage for ρ_L and ρ_M, respectively. Following Sn deposition, the sample was transferred into the preparation chamber for AES analysis to characterize the surface composition and/or heating at $T_S = 24$, 500, 700, or 850 °C and then transferred into the STM chamber for spatially resolved analysis of sub-ML adlayers on the ρ_L and ρ_M (3 × 1)-O Nb(100) samples.

III. RESULTS AND DISCUSSION

Following preparation of the ρ_P (3 × 1)-O Nb(100) under UHV conditions, the ever-present NbO surface oxide reconstructs into a ladder structure as previously characterized.[20,21,23,24] Characterization of the chemical composition of the ρ_P, ρ_L, and ρ_M NbO/Nb(100) surfaces *via* AES, shown in Fig. 1, confirms comparable Nb, Sn, and O peak intensities for each sample preparation. Both ρ_L and ρ_M samples require either an anneal or flash to $T_S = 900$ °C after sputtering procedures due to bulk carbon contaminants present on the surface following Ar^+ sputtering; the ρ_L and ρ_M samples show no evidence of contaminant incorporation upon completion of sample preparation methods. It is known that O diffuses into the Nb bulk upon heating and diffuses to the surface and near-surface region of the crystal upon sample cooling, allowing for the regular reformation of stable Nb_xO_y phases.[20,23,25,26] Therefore, it is not possible to determine whether O or Nb is preferentially sputtered from the (3 × 1)-O Nb(100) surface following ρ_L or ρ_M sample preparation.[27] A representative AES survey spectrum of the ρ_M sample with 16.77 ML equivalence of Sn deposited at $T_S = 24$ °C shows no evidence of contamination following Sn deposition procedures.

While AES analysis of the ρ_P, ρ_L, and ρ_M samples confirms chemical composition and cleanliness of the prepared surfaces, STM is needed to provide spatially resolved structural information of the intentionally defected NbO/Nb(100) surfaces. A representative STM image of the ρ_P (3 × 1)-O surface is shown in Fig. 2(a). The surface is comprised of large, flat terraces with crisp step edges and minimal NbO adatoms; body-centered cubic NbO adatoms display as bright rectangular protrusions from the Nb(100) terrace. The ρ_L sample, shown in Fig. 2(b), has visibly narrowed terraces with NbO adatoms uniformly protruding across the surface. The

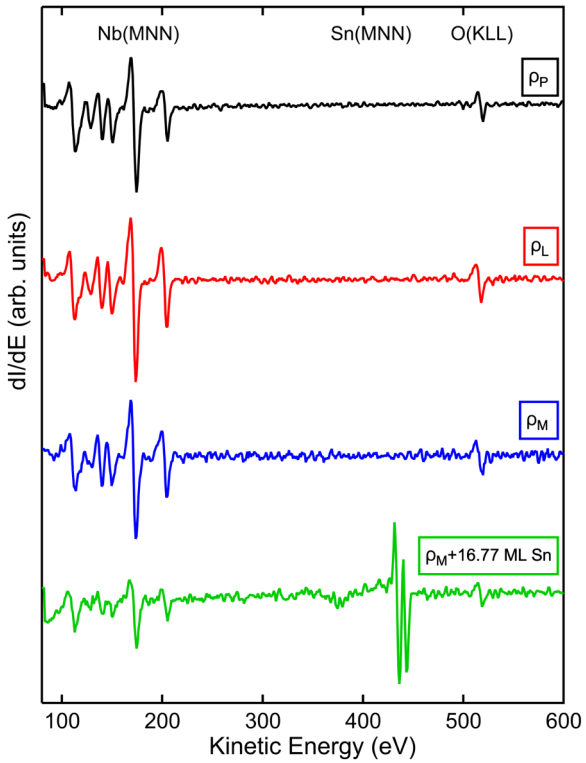

FIG. 1. AES spectra of the pristine (ρ_P), low defect density (ρ_L), moderate defect density (ρ_M), and ρ_M surface with 16.77 ML equivalence of Sn (ρ_M + 16.77 ML Sn) deposited at $T_S = 24$ °C. There is no evidence of surface contamination following the low defect density or moderate defect density sample preparation nor following Sn deposition. The ρ_L and ρ_M spectra have 11.5 and 12.3 O at. %, respectively.

ρ_M sample, shown in Fig. 2(c), is the most visually defected surface, containing the highest concentration of NbO adatoms from the (3 × 1)-O terraces. The quantity of surface defects resulting from terrace reconstructions on the ρ_M surface inhibits the identification of discrete terraces and step edges from STM line scans.

The defect density of each (3 × 1)-O Nb(100) surface preparation was obtained by identifying edge corrugation resulting from NbO step edges, adatoms, and pits. Despite the varying defect densities across the three sample preparations, the underlying ρ_P, ρ_L, and ρ_M NbO oxide structure is consistent with the characteristic (3 × 1)-O ladder structure. Figure 2(d) shows the quantified surface area attributable to edge sites for each sample preparation, revealing that the ρ_P, ρ_L, and ρ_M surfaces have unique defect densities. Edge sites comprise 4.6 ± 1.9% of the ρ_P surface, 17.8 ± 1.2% of the ρ_L surface, and 31.3 ± 2.1% of the ρ_M surface. The development of the ρ_L and ρ_M surface preparation methods allows for a highly reproducible method to impart nanoscale defects on the (3 × 1)-O Nb (100) surface. The difference in defect density between the ρ_P, ρ_L, and ρ_M surfaces, while maintaining an identical (3 × 1)-O unit cell, enables the investigation of Sn adsorption and diffusion behavior solely as a function of nanoscale structural defects.

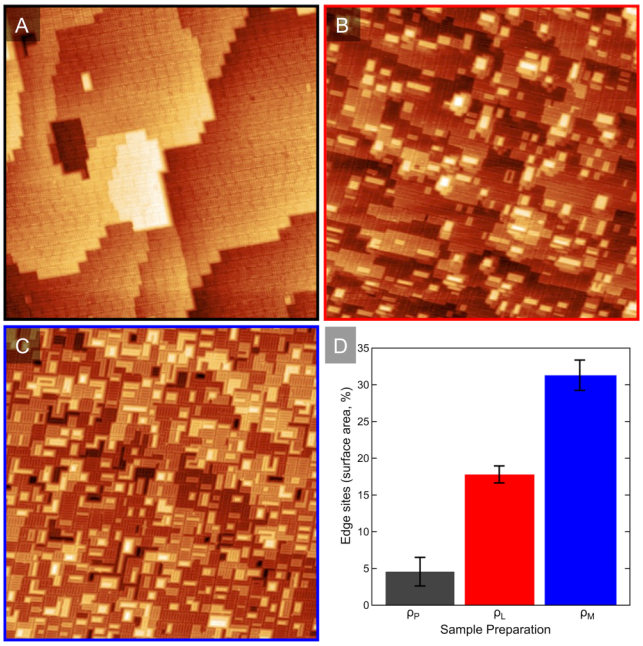

FIG. 2. Room temperature STM images (125 × 125 nm^2) of the (a) pristine (ρ_P) (3 × 1)-O/Nb(100) surface 181 mV, 177 pA; (b) low defect density (ρ_L) (3 × 1)-O/Nb(100) surface −392 mV, −102 pA; (c) moderate defect density (ρ_M) (3 × 1)-O/Nb(100) surface −0.75 V, −148 pA; and (d) quantification of the edge sites present on each respective surface as determined by the surface area marked as an edge site. Error bars denote standard error resulting from three averaged edge site calculations. ρ_P: 4.6 ± 1.9%, ρ_L: 17.8 ± 1.2%, and ρ_M: 31.3 ± 2.1%.

Sufficiently low coverages of Sn must be deposited onto the (3 × 1)-O surface to determine the interatomic forces guiding Sn adsorption and diffusion behavior on the intentionally defected (3 × 1)-O surfaces. This allows for the simultaneous visualization of adsorbed Sn adatoms and the underlying (3 × 1)-O ladder structure, providing necessary information on the interactions between Sn and the edge sites, adatoms, pits, and terraces of the (3 × 1)-O surface. AES spectra for the undosed and dosed ρM sample (Fig. 1) show only Nb MNN, Sn MNN, and O KLL peaks with no evidence of surface contaminants resulting from either the sample preparation or Sn deposition. Therefore, any features that are not inherently attributable to the underlying (3 × 1)-O surface are attributed to adsorbed Sn atoms.

Figure 3(a) shows an STM image of the ρ_L sample following exposure to 0.28 ML equivalence Sn at $T_S = 24$ °C. The EFM 3 evaporator source produces a flat top diameter Sn evaporant profile, which uniformly deposits on the entire Nb crystal. $SnCl_2$ is used as a nucleating agent in Nb_3Sn film growth procedures and results in Sn nucleation sites leading to uniform Sn adsorption, adlayer formation, and wetting for subsequent Nb_3Sn growth processes.[16–18] $SnCl_2$ readily decomposes upon contact with the Nb cavity surface at 500 °C, resulting in adsorbed Sn which serves as the nucleation site.[16] The work presented herein utilizes metallic Sn, rather than $SnCl_2$, as a model system to understand the behavior of adsorbed Sn on the oxidized Nb surface. There may be differences in the adsorption behavior of $SnCl_2$ and metallic Sn, which will be probed in future work.

Sn adatoms, visualized as bright protrusions, are seen to preferentially align along the edges of the (3 × 1)-O ladders following Sn exposure at $T_S = 24$ °C. While there is evidence of Sn aggregation on the ρ_L surface upon deposition, there is no evidence that Sn is preferentially diffusing to larger scale defects such as step edges. Rather, Sn aligns with the edges of the (3 × 1)-O ladder structure between ladder columns. Similar behavior has been observed for sub-ML quantities of Pd, Rh, and Ir deposited onto a thin alumina film at 300 K.[28] It has also been shown that for other planar metal oxides, such as MgO(001), transition metal adatoms and small clusters may diffuse *via* hopping among oxygen sites at or below 24 °C.[29–32]

In addition to hopping, adatoms on planar metal oxides at or below $T_S = 24$ °C may undergo long jumps to a site that is not the nearest neighbor of the initial adsorption site.[33–36] The probability of a long jump is dependent on a dissipation parameter, Δ, which is based on the ratio between the energy loss in crossing a single lattice spacing and the thermal energy, k_BT.[37–39] The observed behavior of Sn preferentially adsorbing along the edge sites of (3 × 1)-O Nb(100) ladder rows may therefore be due to room temperature hopping and long jump behavior of Sn on ρ_L. Further computational models of Sn adsorption and diffusion behavior on (3 × 1)-O Nb(100) are needed to fully rationalize the energetics and mechanisms of Sn adsorption and diffusion on oxidized Nb at room temperature.

The 0.28 ML/ρ_L sample was then annealed at $T_S = 500$ °C for 15 min and analyzed *via* STM as shown in Fig. 3(b). Upon annealing at $T_S = 500$ °C, Sn coalesces into long islands that stretch across terraces and are confined between the (3 × 1)-O ladders. Despite the presence of some NbO adatoms, Sn does not preferentially aggregate at these edge sites or terrace step edges. Rather, the underlying (3 × 1)-O oxide structure directly influences Sn island formation along the (3 × 1)-O unit cell with no clear preference for adsorption to surface defects such as edge sites.

Annealing at $T_S = 700$ °C for 15 min results in the formation of larger Sn islands spanning entire terraces of the (3 × 1)-O surface, as shown in Fig. 3(c). The Sn islands blanket the terraces with no clear drive to diffuse toward defect sites as an initial adsorption site. Following a 15 min anneal at $T_S = 850$ °C, all Sn has desorbed from ρ_L, as confirmed by AES, and the surface shows evidence of returning to a pristine (3 × 1)-O surface [Fig. 3(d)]. Despite having 17.8 ± 1.2% relative surface area of edge sites on the (3 × 1)-O surface, Sn adsorption and diffusion behavior is more directly influenced by the underlying ladder surface structure than the increased presence of edge sites.

With an understanding that Sn adsorption and diffusion behavior is unaffected at defect densities ≤18%, the defect density of the surface was increased to 31.3 ± 2.1% (ρ_M). ρ_M was exposed to 0.24 ML equivalence of Sn at $T_S = 24$ °C and analyzed *via* room temperature STM. Unlike ρ_L, Sn is uniformly adsorbed on the ρ_M surface following deposition at $T_S = 24$ °C, as shown in Fig. 3(e). While there is some evidence of directionality in the Sn adsorbate structure, the corrugation of the ρ_M surface resulting in uniform Sn adsorption across the surface makes distinguishing between

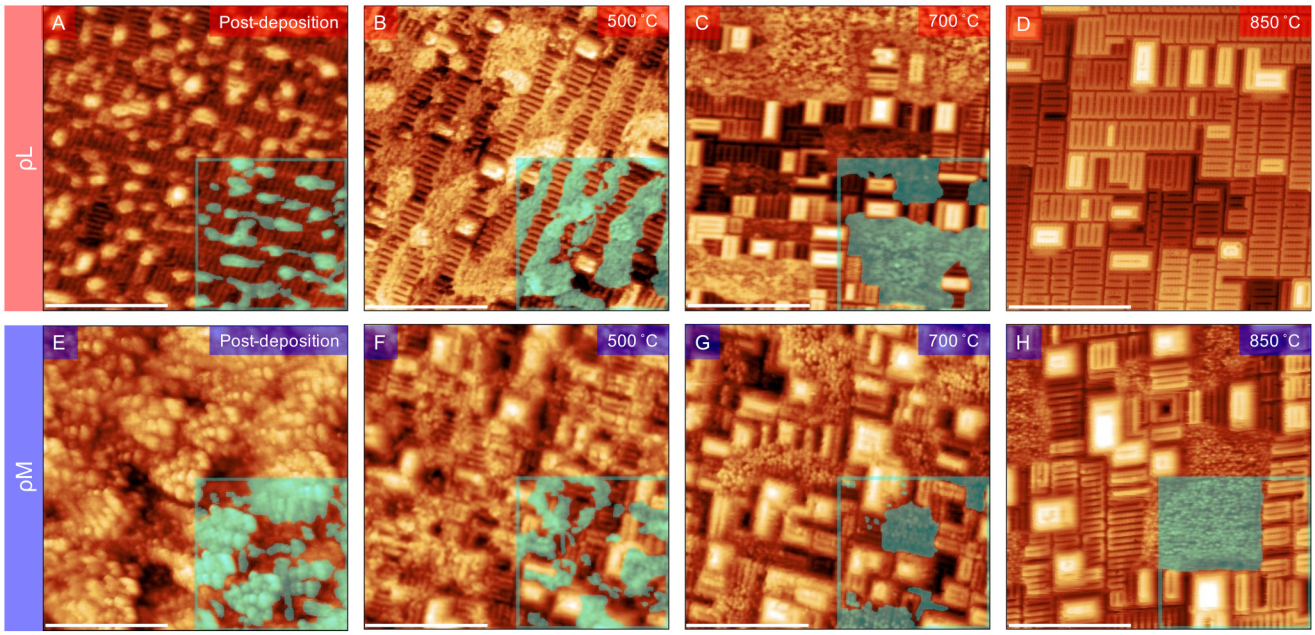

FIG. 3. Visualization of Sn adsorption and diffusion behavior on low defect density (ρ_L) and moderate defect density (ρ_M) (3 × 1)-O/Nb(100) via room temperature STM (scale bar = 20 nm, 50 × 50 nm^2). Samples annealed for 15 min at each temperature. A representative region of adsorbed Sn is masked in the lower right hand corner of each image. (a) 0.28 ML equivalence Sn deposition at T_S = 24 °C. Sn adsorbs along the (3 × 1)-O ladder structure. 344 mV, 141 pA; (b) T_S = 500 °C. Sn aggregates along the ladder structure and not at edge sites −0.70 V, −105 pA; and (c) T_S = 700 °C. Sn forms larger islands with no evidence of preference for nanoscale defects. −388 mV, −83 pA; (d) T_S = 850 °C. Sn desorbs by T_S = 850 °C −331 mV, −108 pA; (e) 0.24 ML equivalence Sn deposition at T_S = 24 °C. Sn adsorbs as bright features across the entire surface with some alignment with (3 × 1)-O ladders −144 mV, −149 pA; (f) T_S = 500 °C. Sn diffuses to ladder structure edges −438 mV, −205 pA; (g) T_S = 700 °C. Sn forms larger islands with no evidence of preference for nanoscale defects 0.75 V, 119 pA; (h) anneal at T_S = 850 °C. Sn forms large islands and does not desorb −0.81 V, −125 pA.

adsorbed Sn atoms and the underlying (3 × 1)-O ladder structure technically difficult. Complementary AES confirms deposition of 0.24 ML equivalence of Sn on the surface; the difference in Sn adsorption behavior is not due to excess Sn on the ρ_M surface. The difference in Sn adsorption is, therefore, attributable to the higher defect density on the ρ_M surface. The hopping and long jump behavior that is seen on planar metal oxides may be disrupted by the increase in surface defects on the ρ_M sample, which act as trapping sites, leading to no obvious Sn ordering on the ρ_M surface following Sn deposition at T_S = 24 °C.[40–43]

Upon annealing the 0.24 ML Sn/ρ_M surface at T_S = 500 °C for 15 min, the underlying (3 × 1)-O ladders are again visible as well as small, bright clusters of Sn adatoms [Fig. 3(f)]. While the Sn adsorbate structure in Fig. 3(b) shows columns of Sn along the (3 × 1)-O ladder edges, the Sn adsorbate islands in Fig. 3(f) are much smaller in length and have a less obvious association with (3 × 1)-O ladder edge sites. This may be due to the increased defect density and surface corrugation resulting in shorter terrace widths, displaced NbO resulting in pits, or the much larger NbO protrusions across the surface. Annealing at T_S = 700 °C for 15 min, however, results in Sn adsorbate structures [Fig. 3(g)] that are visually similar to those observed after annealing the 0.28 ML Sn/ρ_L sample at T_S = 700 °C for 15 min. The 0.24 ML/ρ_M sample shows larger islands of Sn adsorbates occupying areas of the (3 × 1)-O terraces with no obvious preference for edge sites. Within the Sn islands, there are regions of squarelike and hexagonal-like packing visible among the protruding Sn atoms. These atomically resolved structures are similar to proposed atomic arrangements of Sn on metallic Nb(110) corresponding to $c(3 \times 1)$, hexagonal-like, and $p(1 \times 1)$, squarelike, low energy electron diffraction patterns.[44]

Upon annealing at T_S = 850 °C for 15 min, shown in Fig. 3(h), the ρ_M surface appears to have flattened relative to lower temperature annealing points and there are several large Sn islands scattered across the surface. These larger Sn islands span the width of the (3 × 1)-O terraces with little evidence for preferential diffusion toward edge sites. The concomitant formation of larger Sn islands as the surface defects anneal out suggests that larger Sn structures can only form in the presence of fewer surface defects. This may explain experimental results that show Sn rich and poor regions in Nb_3Sn films grown on polycrystalline Nb SRF cavities.[10,13,16,19] Smoother, less structurally defected Nb surfaces may be required for uniform Sn diffusion on Nb surfaces prior to Sn incorporation or alloy formation.

The STM data presented in Fig. 3, which provide novel information regarding Sn adsorption, diffusion, and desorption data on the ρ_L and ρ_M surface, are summarized as follows:

Sn deposited at $T_S = 24$ °C on the ρ_L surface [Fig. 3(a)] shows Sn preferentially adsorbing along the (3 × 1)-O ladders while Sn deposited on the ρ_M surface [Fig. 3(e)] shows uniform Sn coverage with no clear preference for ladder edge sites or surface defects. Annealing at $T_S = 500$ and 700 °C induces Sn diffusion along the (3 × 1)-O ladder edges on both the ρ_L and ρ_M surfaces and the formation of comparable squarelike and hexagonal-like Sn surface structures [Figs. 3(b), 3(c), 3(f), and 3(g)]. Annealing at $T_S = 850$ °C results in complete Sn desorption from the ρ_L surface while regions of residual Sn persist on the ρ_M surface [Figs. 3(d) and 3(h)]. These data reveal that, while an increase in surface defects disrupts ordering of Sn adsorbates along the (3 × 1)-O ladder edges upon adsorption at room temperature, the overall diffusion pathway of Sn on the ρ_L and ρ_M surface is not influenced by an increase in surface defect density. Rather, the underlying oxide composition and structure is a more direct influence on Sn diffusion behavior. There is, however, enhanced thermal stability for adsorbed Sn on ρ_M, suggesting that surface defects may stabilize Sn at elevated temperatures during Nb_3Sn growth procedures. Including the oxidized Nb surface composition and structure is, therefore, essential in developing more representative predictive growth models for optimal Nb_3Sn films.

To compare the surface and near-surface elemental composition on the defect-induced (3 × 1)-O Nb(100) surfaces, AES was employed to investigate the surface chemical compositions following exposure to lower (Sn ≤ 0.5 ML) and higher (15 ≤ Sn ≤ 20 ML) Sn exposures at $T_S = 24$ °C. As described in Sec. II, sub-ML and multilayer coverages of Sn were deposited at 0.47–0.56 and 0.80–0.84 ML min^{-1}, respectively. Proportions of the Nb, Sn, and O dI/dE peak-peak heights, corrected with sensitivity factors, yield the relative surface and near-surface composition (at. %). As shown in Fig. 4, the Nb, Sn, and O at. % of the ρ_P surface evolves in a linear manner with calibrated ML Sn coverage. Calibration of the ML deposition rate at varying evaporation conditions accounts for both the ng/min deposition rate, as determined by QCM measurements, and the Sn surface packing density on ρ_P, visualized via atomically resolved STM image mapping.

The Sn at. % has a linear relationship with the ML of Sn exposed during room temperature deposition on ρ_P. For both Sn coverage regimes displayed in Fig. 4, the Nb, O, and Sn at. % on the ρ_L and ρ_M surfaces fits within the error of the ρ_P experimental data. In conjunction with the STM data shown in Fig. 3, these results suggest that, while the diffusion pathways may be influenced by increased surface defect densities, the at. % of the Sn/(3 × 1)-O is not significantly altered by nanoscale surface defects. Further investigations into the effect of grain boundaries on initial Sn adsorption and diffusion behavior are needed to build a more complete understanding of the role of structural defects on alloying behavior of polycrystalline oxidized Nb surfaces.

The Nb at. % following Sn deposition on the ρ_P surface follows a linear decay as a function of Sn coverage. The detected O is bound to Nb in the (3 × 1)-O surface oxide, and while a proportional decrease in O may be expected, the O at. % remains constant for all Sn ML coverages investigated. AES signal attenuation due to ideal ML deposition can be estimated by calculating the signal loss (I_X/I_X^0),[45] which is dependent on the Sn adlayer thickness (d), inelastic mean free path (λ),[46] and the angle between the analyzer and the sample (θ). If it is assumed that Sn deposition follows

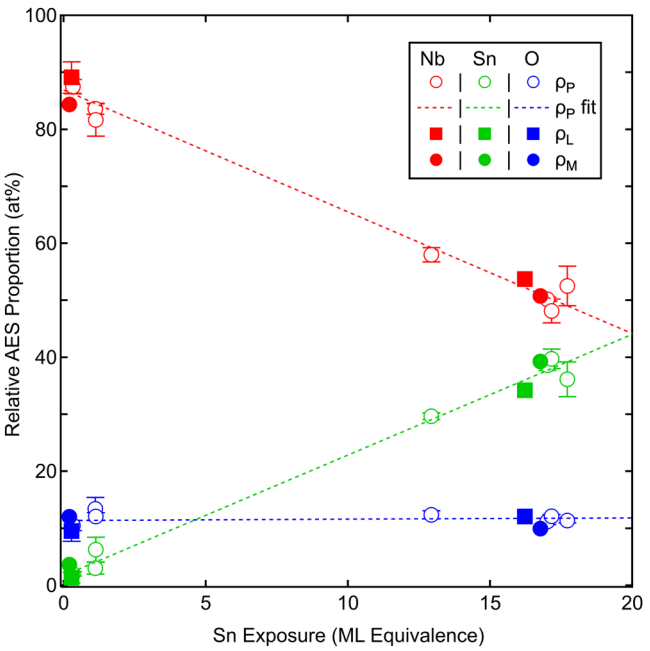

FIG. 4. Proportions of the corrected peak-peak heights in the differential AES survey spectra, denoted as atomic percentages (at. %) of Nb, Sn, and O, following Sn deposition on ρ_P ρ_L, ρ_M (3 × 1)-O/Nb(100) at $T_S = 24$ °C. Linear fit, indicated by dashed lines, for Sn deposition on ρ_P (3 × 1)-O/Nb(100) span both lower (Sn ≤ 0.5 ML) and higher (15 ≤ Sn ≤ 20 ML) coverage regimes. AES proportions following Sn deposition on ρ_L and ρ_M surfaces indicate that the surface composition following room temperature Sn deposition is not impacted by the increasing nanoscale surface defects.

either an ML or hybrid ML-island growth mechanism, the measured Nb AES signal would decay into the background signal above ~10 ML. As there is not a substantial loss of Nb AES signal beyond ~10 ML Sn deposition, there is likely Sn island formation rather than strictly ML growth, with Sn-Sn adlayer interactions dominating at higher coverages. Sn island formation at higher coverages, as opposed to uniform surface wetting, likely explains the detection of the Nb and O signals even at multilayer coverages, with regions of the underlying (3 × 1)-O surface still within the AES detection escape depth.

Sn island growth does not, however, explain the near-constant O at. % with a concomitant decay in Nb at. % at higher Sn coverages. This consistent O signal intensity at high Sn coverages may, in part, be accounted for by the considerably greater escape depth of O KLL electrons compared to Nb MNN electrons;[46] some oxygen migration from the underlying Nb to the Sn adlayer phase may also occur. Further studies aim to elucidate the sub-ML and multilayer Sn growth behavior on (3 × 1)-O Nb(100) due to varying substrate conditions such as sample temperature, oxide composition and structure, and crystallographic orientation as these initial Sn/Nb/O interactions play a significant role in determining the eventual homogeneity of Nb_3Sn thin films.

IV. SUMMARY AND CONCLUSIONS

We report the first *in situ* atomic-scale visualization of Sn adsorption and diffusion behavior on well characterized ρ_L and ρ_M (3×1)-O Nb(100) surfaces. Room temperature STM analysis reveals that Sn preferentially aligns along the (3×1)-O ladder edges following deposition at $T_S = 24$ °C on the ρ_L surface. On the ρ_M surface, Sn adsorbs uniformly across the surface at $T_S = 24$ °C with some directional uniformity in the Sn adlayer. For both the ρ_L and ρ_M surfaces, annealing at $T_S = 500$ and 700 °C results in Sn diffusion along the (3×1)-O ladder edges and the formation of Sn islands comprised of squarelike and hexagonal-like structures. By $T_S = 850$ °C, there is complete Sn desorption from the ρ_L surface while Sn islands are still present on the ρ_M surface. The increased defect density of the ρ_M surface stabilizes Sn adsorbates at elevated temperatures and suggests that higher defect densities may stabilize Sn adsorbates at elevated temperatures during Nb_3Sn growth procedures. Despite the variation in atomistic adsorption and diffusion mechanisms, there is no variation in the surface composition at $T_S = 24$ °C, as shown *via* complementary, *in situ* AES analysis. This work provides necessary atomic-scale information regarding the effect of structural defects on Sn adsorption and diffusion behavior and our findings indicate that Sn adsorption and diffusion pathways are primarily dependent on the underlying Nb oxide structure and not solely driven by structural defects. Further experimental and computational studies are needed to understand the relationship between nanoscale defects, surface crystallographic orientation, oxidation state of the Nb surface, and Sn deposition conditions on Sn adsorption, diffusion, and alloy growth behavior. These findings represent new atomic-level information that will contribute to the development of more accurate and predictive Nb_3Sn growth models.

ACKNOWLEDGMENTS

This work was supported by the U.S. National Science Foundation under Award No. PHY-1549132, the Center for Bright Beams, and NSF Materials Research Science and Engineering Center (MRSEC) at the University of Chicago, Grant No. NSF-DMR-2011854. R.G.F. thanks the University of Chicago for partial support via the Kadanoff-Rice Fellowship during this work.

DATA AVAILABILITY

The data that support the findings of this study are available within the article.

REFERENCES

[1]H. Padamsee and J. Knobloch, *RF Superconductivity for Accelerators* (Wiley-VCH, New York, 2008).
[2]H. Padamsee, *RF Superconductivity: Science, Technology, and Applications* (John Wiley & Sons, Weinheim, 2009).
[3]C. Antoine, *Materials and Surface Aspects in the Development of SRF Niobium Cavities*, EuCARD Editorial Series on Accelerator Science (CERN, Meyrin, Switzerland, 2012); available at http://cdsweb.cern.ch/record/1472363.
[4]S. Posen and D. L. Hall, Supercond. Sci. Technol. **30**, 033004 (2017).
[5]N. Stilin, A. Holic, M. Liepe, R. Porter, and J. Sears, "Stable CW operation of Nb_3Sn SRF cavity at 10 MV/m using conduction cooling," arXiv:2002.11755 [physics] (2020).
[6]S. Posen, M. Liepe, and D. L. Hall, Appl. Phys. Lett. **106**, 082601 (2015).
[7]H. Heinrichs, G. Arnolds-Mayer, T. Grundey, U. Klein, N. Minatti, G. Muller, M. Peiniger, H. Piel, G. Unterborsch, and H. P. Vogel, "Activities on RF-superconudctivity at Wuppertal," in *Proceedings of the Second Workshop on Rf-Superconductivity*, Geneva, Switzerland, 23–27 July (CERN, Meyrin, Switzerland, 1984), pp. 141–170.
[8]M. Peiniger, *Herstellung Und Test Eines S-Band Resonators Mit Nb_3Sn Oberflache* (Universitat Gesamthochschule Wuppertal, Wuppertal, 1983).
[9]M. Peiniger, M. Hein, N. Klein, G. Muller, H. Piel, and P. Thuns, "Work on Nb_3Sn cavities at Wuppertal," in *Proceedings of the Third Workshop on RF Superconductivity*, Argonne, IL, 14–18 September 1987 (Argonne National Laboratory, Lemont, IL, 1988), pp. 503–531.
[10]J. Lee, S. Posen, Z. Mao, Y. Trenikhina, K. He, D. L. Hall, M. Liepe, and D. N. Seidman, Supercond. Sci. Technol. **32**, 024001 (2018).
[11]M. M. Kelley, N. S. Sitaraman, and T. A. Arias, Supercond. Sci. Technol. **34**, 015015 (2021).
[12]N. S. Sitaraman, M. M. Kelley, R. D. Porter, M. U. Liepe, T. A. Arias, J. Carlson, A. R. Pack, M. K. Transtrum, and R. Sundararaman, Phys. Rev. B **103**, 115106 (2021).
[13]S. Posen, J. Lee, D. N. Seidman, A. Romanenko, B. Tennis, O. S. Melnychuk, and D. A. Sergatskov, Supercond. Sci. Technol. **34**, 025007 (2021).
[14]U. Pudasaini, M. J. Kelley, G. Ciovati, G. V. Eremeev, C. E. Reece, I. P. Parajuli, and N. Sayeed, "Recent results from Nb_3Sn single cell cavities coated at Jefferson lab," in *Proceedings of the 9th International Particle Accelerator Conference (IPAC2018)*, Vancouver, BC, 29 April–4 May 2018, http://www.jacow.org, pp. 1798–1803.
[15]D. L. Hall, "New insights into the limitations on the efficiency and achievable gradients in Nb_3Sn SRF cavities," Ph.D. thesis (Cornell University, 2017).
[16]U. Pudasaini, G. V. Eremeev, C. E. Reece, J. Tuggle, and M. J. Kelley, "Surface studies of Nb_3Sn coated samples prepared under different coating conditions," in *18th International Conference on RF Superconductivity*, Lanzhou, China, 17–21 July 2017, http://www.jacow.org, pp. 894–899.
[17]U. Pudasaini, G. V. Eremeev, J. W. Angle, J. Tuggle, C. E. Reece, and M. J. Kelley, J. Vac. Sci. Technol. A **37**, 051509 (2019).
[18]S. Posen and M. Liepe, Phys. Rev. Spec. Top.--Accel. Beams **17**, 112001 (2014).
[19]J. Lee *et al.*, Acta Mater. **188**, 155 (2020).
[20]R. D. Veit, N. A. Kautz, R. G. Farber, and S. J. Sibener, Surf. Sci. **688**, 63 (2019).
[21]B. An, S. Fukuyama, K. Yokogawa, and M. Yoshimura, Phys. Rev. B **68**, 115423 (2003).
[22]R. D. Veit, R. G. Farber, N. S. Sitaraman, T. A. Arias, and S. J. Sibener, J. Chem. Phys. **152**, 214703 (2020).
[23]A. A. McMillan, J. D. Graham, S. A. Willson, R. G. Farber, C. J. Thompson, and S. J. Sibener, Supercond. Sci. Technol. **33**, 105012 (2020).
[24]Y. Li, B. An, S. Fukuyama, K. Yokogawa, and M. Yoshimura, Mater. Charact. **48**, 163 (2002).
[25]M. Grundner and J. Halbritter, J. Appl. Phys. **51**, 397 (1980).
[26]H. Oechsner, J. Giber, H. J. Füßer, and A. Darlinski, Thin Solid Films **124**, 199 (1985).
[27]E. Atanassova, T. Dimitrova, and J. Koprinarova, Appl. Surf. Sci. **84**, 193 (1995).
[28]M. Frank and M. Bäumer, Phys. Chem. Chem. Phys. **2**, 3723 (2000).
[29]R. Ferrando and A. Fortunelli, J. Phys.: Condens. Matter **21**, 264001 (2009).
[30]G. Barcaro and A. Fortunelli, New J. Phys. **9**, 22 (2007).
[31]G. Barcaro, A. Fortunelli, F. Nita, and R. Ferrando, Phys. Rev. Lett. **95**, 246103 (2005).
[32]L. Xu, G. Henkelman, C. T. Campbell, and H. Jónsson, Phys. Rev. Lett. **95**, 146103 (2005).
[33]R. Ferrando, R. Spadacini, and G. E. Tommei, Phys. Rev. E **48**, 2437 (1993).
[34]T. Ala-Nissila, R. Ferrando, and S. C. Ying, Adv. Phys. **51**, 949 (2002).
[35]S. Miret-Artés and E. Pollak, J. Phys.: Condens. Matter **17**, S4133 (2005).
[36]G. Antczak and G. Ehrlich, Surf. Sci. Rep. **62**, 39 (2007).

[37]V. I. Mel'nikov, Phys. Rep. **209**, 1 (1991).
[38]R. Ferrando, R. Spadacini, G. E. Tommei, and G. Caratti, Surf. Sci. **311**, 411 (1994).
[39]R. Ferrando, R. Spadacini, G. E. Tommei, and G. Caratti, Physica A **195**, 506 (1993).
[40]L. Xu and G. Henkelman, Phys. Rev. B **77**, 205404 (2008).
[41]C. Ratsch and J. A. Venables, J. Vac. Sci. Technol. A **21**, S96 (2003).
[42]J. W. Evans, P. A. Thiel, and M. C. Bartelt, Surf. Sci. Rep. **61**, 1 (2006).
[43]A. Bogicevic and D. R. Jennison, Surf. Sci. **515**, L481 (2002).
[44]J. A. Strozier, D. L. Miller, O. F. Kammerer, and M. Strongin, J. Appl. Phys. **47**, 1611 (1976).
[45]I. S. Tilinin, A. Jablonski, and W. S. M. Werner, Prog. Surf. Sci. **52**, 193 (1996).
[46]C. J. Powell and A. Jablonski, *NIST Electron Inelastic-Mean-Free-Path Database - Version 1.2* (National Institute of Standards and Technology, Gaithersburg, MD, 2010).